

# Bi<sub>12</sub>O<sub>17</sub>Cl<sub>2</sub>/(BiO)<sub>2</sub>CO<sub>3</sub> Nanocomposite Materials for Pollutant Adsorption and Degradation: Modulation of the Functional Properties by Composition Tailoring

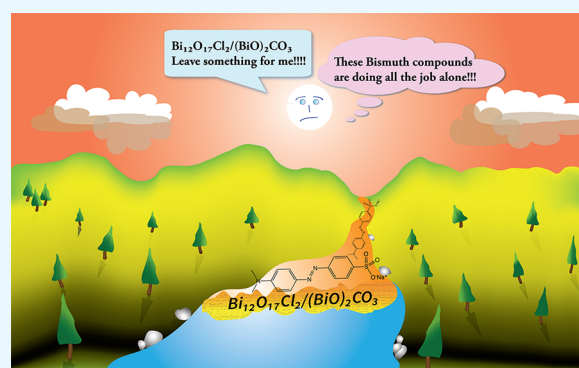
Federica Mian,<sup>†</sup> Gregorio Bottaro,<sup>\*,†</sup> Marzio Rancan,<sup>†</sup> Luigi Pezzato,<sup>‡</sup> Valentina Gombac,<sup>\*,§</sup> Paolo Fornasiero,<sup>§</sup> and Lidia Armelao<sup>†,‡</sup>

<sup>†</sup>ICMATE-CNR and INSTM, c/o Department of Chemical Sciences, University of Padova, Via F. Marzolo 1, 35131 Padova, Italy

<sup>‡</sup>Department of Chemical Sciences, University of Padova, Via F. Marzolo 1, 35131 Padova, Italy

<sup>§</sup>Department of Chemical and Pharmaceutical Sciences, ICCOM-CNR Trieste Research Unit and INSTM, University of Trieste, Via L. Giorgieri 1, 34127 Trieste, Italy

**ABSTRACT:** Bi<sub>12</sub>O<sub>17</sub>Cl<sub>2</sub>/(BiO)<sub>2</sub>CO<sub>3</sub> nanocomposite materials were studied as bifunctional systems for depuration of wastewater. They are able to efficiently adsorb and decompose rhodamine B (RhB) and methyl orange (MO), used as model pollutants. Bi<sub>12</sub>O<sub>17</sub>Cl<sub>2</sub>/(BiO)<sub>2</sub>CO<sub>3</sub> nanocomposites were synthesized at room temperature and ambient pressure by means of controlled hydrolysis of BiCl<sub>3</sub> in the presence of a surfactant (Brij 76). Cold treatments of the pristine samples with UV light or thermal annealing at different temperatures (370–500 °C) and atmospheres (air, Ar/30% O<sub>2</sub>) were adopted to modulate the relative amounts of Bi<sub>12</sub>O<sub>17</sub>Cl<sub>2</sub>/(BiO)<sub>2</sub>CO<sub>3</sub> and hence the morphology, surface area, ζ-potential, optical absorption in the visible range, and the adsorption/degradation of pollutants. The best performance was achieved by (BiO)<sub>2</sub>CO<sub>3</sub>-rich samples, which adsorbed 80% of MO and decomposed the remaining 20% by visible light photocatalysis. Irrespective of the dye, all of the samples were able to almost complete the adsorption step within 10 min contact time. Bi<sub>12</sub>O<sub>17</sub>Cl<sub>2</sub>-rich composite materials displayed a lower adsorption ability, but thanks to the stronger absorption in the visible range they behaved as more effective photocatalysts. The obtained results evidenced the ability of the employed strategy to modulate sample properties in a wide range, thus pointing out the effectiveness of this approach for the synthesis of multifunctional inorganic materials for environmental remediation.



## INTRODUCTION

The interest toward multifunctional materials has continuously increased over the last few years. Materials capable of pollutant adsorption and degradation at the same time are highly desirable for environmental remediation strategies. Among the most widespread pollutants, dyes represent a considerable portion because they are employed in different areas, including textile, dyeing, paper and pulp, tannery and paint industries. It has been reported that 10–15% of industrial dyes are lost through wastes.<sup>1</sup> They are considered as particularly offensive pollutants because of their toxicity due to oral ingestion, inhalation, skin and eye irritation, and carcinogenicity.<sup>2–5</sup> Even in low amounts, they may impart color to water. This not only is unpleasant but also affects the transmission of light, thus distressing biological metabolism and leading to destruction of the aquatic communities.<sup>6,7</sup> Moreover, dyes are able to strongly bond heavy metals, causing microtoxicity to fish and other organisms.<sup>7</sup>

For these reasons, the development of strategies to rapidly remove this class of contaminants from wastewater and/or for their degradation is a fundamental target for environmental protection and remediation. In general, dyes are very difficult to

remove because most of them are resistant to several depuration methods.<sup>8–14</sup> On the contrary, adsorption has been demonstrated to be a suitable and effective approach, owing to the simplicity in processing design, easiness in working conditions, low cost and low energy requirements, and insensitivity to toxic substances.<sup>15</sup> In this framework, an innovative approach consists in the development of bifunctional materials endowed with strong adsorption properties and also able to carry out an efficient and complete degradation of the contaminants. In this regard, a wide variety of materials have been tested as dye adsorbents in aqueous solution.<sup>16–19</sup> Most of them, however, have low adsorption capacities or require rather long contact time, up to some days. Therefore, to develop effective adsorbent systems, these problems must be overcome. On the other hand, photocatalysis represents an intriguing solution among green technologies, and it has attracted extensive interest in the fields of water splitting and pollutant degradation.<sup>20–23</sup> In particular,

Received: August 3, 2017

Accepted: September 21, 2017

Published: October 2, 2017

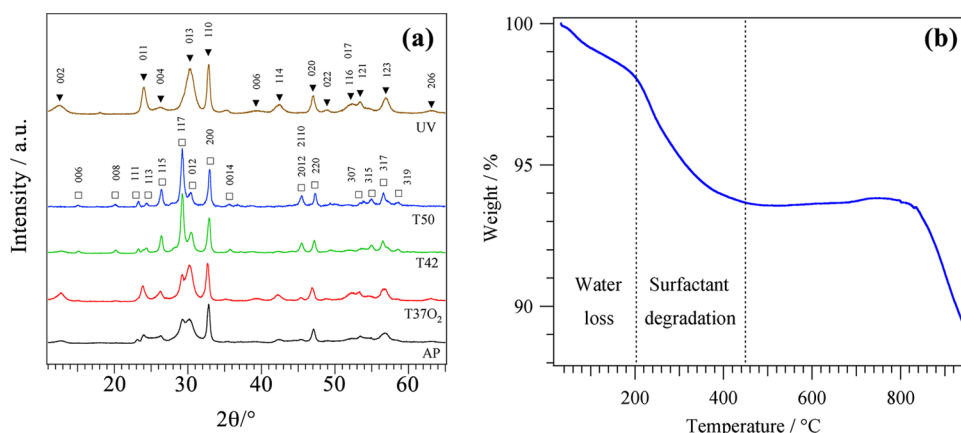


**Figure 1.** (a) XRD patterns of as-prepared and treated  $\text{Bi}_{12}\text{O}_{17}\text{Cl}_2/(\text{BiO})_2\text{CO}_3$  nanocomposite materials. Peculiar diffraction peaks of  $(\text{BiO})_2\text{CO}_3$  ( $\blacktriangledown$ ) and  $\text{Bi}_{12}\text{O}_{17}\text{Cl}_2$  ( $\square$ ) tetragonal phases are labeled. (b) Thermogravimetric analysis (TGA) of the as-prepared sample.

$\text{TiO}_2$  has been recognized as a benchmark photocatalyst for the degradation of organic pollutants in water and wastewater.<sup>24–26</sup> However, the use of titanium oxide and conventional semiconductor photocatalysts is limited by their wide band gap and because they respond only to UV light, which corresponds to less than 5% of sunlight energy.<sup>9</sup> Hence, a further challenge is represented by the development of highly visible light-driven photocatalysts to take advantage of the whole solar radiation spectrum.

Over the last few years, bismuthyl ion ( $\text{BiO}^+$ ) based nanostructures have been studied to develop new adsorbent–photocatalytic systems owing to their peculiar physicochemical properties, layered structures, morphologies, and low toxicity.<sup>27–38</sup> In particular, bismuth oxyhalogenides ( $\text{BiOX}$ ,  $X = \text{Cl}$ ,  $\text{Br}$ ,  $\text{I}$ , and their mixtures) and bismuth subcarbonate,  $(\text{BiO})_2\text{CO}_3$ , nanostructures displayed encouraging performances. Besides  $\text{BiOCl}$ , further bismuth oxychlorides with different stoichiometry, such as  $\text{Bi}_{24}\text{O}_{31}\text{Cl}_{10}$ ,  $\text{Bi}_3\text{O}_4\text{Cl}$ ,  $\text{Bi}_{12}\text{O}_{17}\text{Cl}_2$ , etc., are possible.<sup>39</sup> All of them are characterized by layered structures; can be synthesized with different shapes, that is, nanosheets and nanoflakes; and are active as both adsorbent and photocatalytic materials. Notably, the visible light absorption increases with a decrease in the chlorine content. Besides the single oxychlorides or subcarbonate, the  $\text{BiOCl}/\text{Bi}_2\text{O}_3$ ,  $\text{BiOCl}/\text{BiOI}$ , and  $\text{BiOI}/\text{Bi}_{12}\text{O}_{17}\text{Cl}_2$  composite systems that display heterojunction structures can operate far better than the single components thanks to the presence of synergic effects at the interface between the two phases.<sup>30,40–42</sup> In these structures, oxygen-rich oxychlorides, like for example  $\text{Bi}_{12}\text{O}_{17}\text{Cl}_2$ , and oxyhalides containing  $\text{Br}$  and  $\text{I}$  are used as sensitizers to harvest the visible light, and their effect is particularly important when coupled to materials with low to no visible absorption, as  $\text{BiOCl}$  and  $(\text{BiO})_2\text{CO}_3$ , to form the heterojunction. In this regard, the present study explores the modulation of optical and dye adsorption/photodegradation properties of  $\text{Bi}_{12}\text{O}_{17}\text{Cl}_2/(\text{BiO})_2\text{CO}_3$  nanocomposite materials by tailoring the relative amount of the two components.

The inorganic composites were prepared by a soft solution method and subsequent postsynthesis treatments (thermal and cold UV-light-assisted) to modulate their properties and hence their dye absorption–degradation capability. These functional properties are affected by several factors correlated to both bulk and surface characteristics of the materials. To fully characterize the materials, we employed powder X-ray diffraction, Raman spectroscopy, optical absorption spectroscopy, and X-ray

photoelectron spectroscopy (XPS). Sample morphology was explored by scanning electron microscopy (SEM). Finally, the adsorption capacity (AC) and degradation activity of the  $\text{Bi}_{12}\text{O}_{17}\text{Cl}_2/(\text{BiO})_2\text{CO}_3$  nanocomposite materials under visible light irradiation were tested toward rhodamine B (RhB) and methyl orange (MO), which are largely adopted models for cationic and anionic dyes, respectively.

## RESULTS AND DISCUSSION

The as-prepared (AP) and treated materials were characterized by powder X-ray diffraction (XRD) analysis. Despite the employed mild synthesis conditions (e.g., low temperature and atmospheric pressure) and the absence of any thermal treatment, as-prepared samples showed a pattern with multiple diffraction peaks (Figure 1a). The whole set of peaks can be indexed according to two tetragonal phases  $\text{Bi}_{12}\text{O}_{17}\text{Cl}_2$  (JCPDS card no. 37-0702) and  $(\text{BiO})_2\text{CO}_3$  (bismutite, JCPDS card no. 41-1488).

As-prepared samples were preliminarily studied by thermogravimetric analysis (TGA) to investigate their behavior under heating in air. Indeed, the determination of the specimen response to thermal treatments is important in view of the preparation of pure inorganic nanosystems, with the aim of defining suitable annealing conditions.

The TGA curve of the AP sample (Figure 1b) shows an initial weight decrease below 200 °C, which is assigned to the loss of water adsorbed on the surface of the crude powders. From 200 to 450 °C, we correlate the weight loss to the degradation of the residual surfactant. At a higher temperature, between 450 and 800 °C, we observe weight invariance, whereas the weight loss above 800 °C is attributed to the formation of bismuth oxide. Different postsynthesis treatments were conducted on as-prepared samples, to completely remove the surfactant molecules and to modulate the  $\text{Bi}_{12}\text{O}_{17}\text{Cl}_2/(\text{BiO})_2\text{CO}_3$  ratio in the nanocomposite materials, the morphology, and the light absorption. We performed thermal treatments at 500 °C in air for 1 h, which is close to the lowest temperature for the complete surfactant decomposition. It is well-known that high annealing temperatures are apt to reduce the material surface areas that are important parameters for both adsorption and photodegradation properties. For this reason, we also adopted lower annealing temperatures and increased the treatment duration to aid surfactant degradation and to hamper surface area reduction. To this purpose, we performed the following treatments: (i) at 420 °C for 6 h with a slow heating ramp and (ii) at 370 °C for 6 h

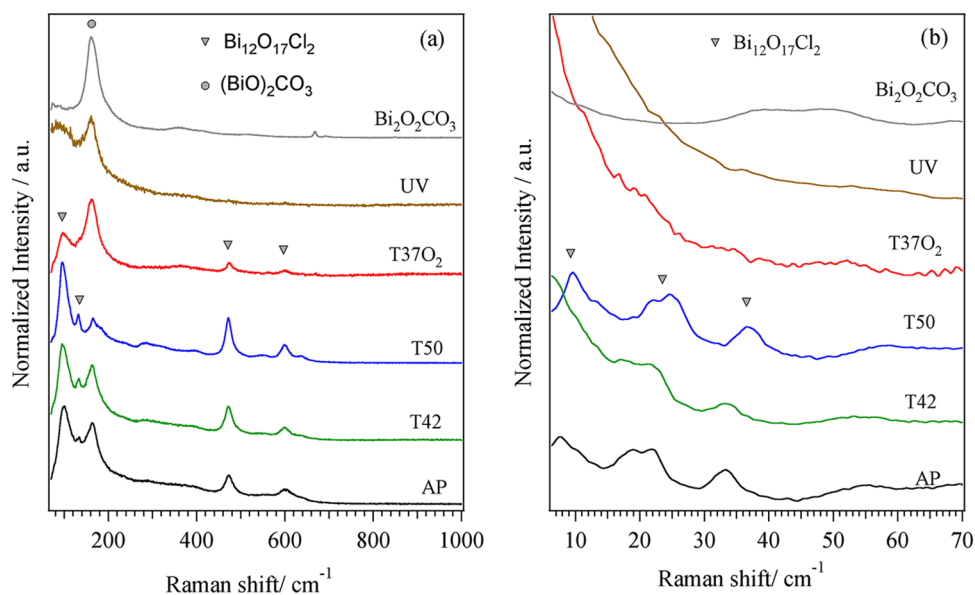


**Figure 2.** (a) Raman spectra of  $\text{Bi}_{12}\text{O}_{17}\text{Cl}_2/(\text{BiO})_2\text{CO}_3$  nanocomposite materials subjected to different annealing procedures. Peaks belonging to  $\text{Bi}_{12}\text{O}_{17}\text{Cl}_2$  and  $(\text{BiO})_2\text{CO}_3$  are indexed in the figure. (b) Low-frequency Raman spectra. Commercial  $(\text{BiO})_2\text{CO}_3$  is used as a reference, and it is displayed in both panels.

in an oxygen-rich atmosphere ( $\text{O}_2$  30% in Ar) to assist the decomposition of the organic moieties that in air at this temperature is not complete (Figure 1b). Moreover, we also carried out a cold annealing procedure by means of UV irradiation at room temperature (up to 14 h) with a medium-pressure Hg lamp. The details of all of the employed treatments are reported in Experimental Section (Table 2).

Postsynthesis treatments strongly influence the nanocomposite structure. The diffraction patterns (Figure 1a) of the annealed samples consist of partially overlapped peaks belonging to  $(\text{BiO})_2\text{CO}_3$  and  $\text{Bi}_{12}\text{O}_{17}\text{Cl}_2$  crystal phases. The strong narrow peak around  $33^\circ$  can be indexed as 200 of  $\text{Bi}_{12}\text{O}_{17}\text{Cl}_2$  as well as 110 of  $(\text{BiO})_2\text{CO}_3$ . Both  $\text{Bi}_{12}\text{O}_{17}\text{Cl}_2$  and  $(\text{BiO})_2\text{CO}_3$  present the typical layered structure of many  $\text{BiO}^+$  compounds.  $(\text{BiO})_2\text{CO}_3$  belongs to the family of Sillén phases in which  $[\text{Bi}_2\text{O}_2]^{2+}$  layers are interleaved with carbonate groups oriented orthogonally to the metal oxide slabs.<sup>43–45</sup> On the other hand, in  $\text{Bi}_{12}\text{O}_{17}\text{Cl}_2$ , chlorine single layers are interleaved with metal oxide sheets.<sup>39,46–48</sup> After annealing, a change in the relative phase amount of  $\text{Bi}_{12}\text{O}_{17}\text{Cl}_2/(\text{BiO})_2\text{CO}_3$  was observed. In fact, the T37O<sub>2</sub> sample was characterized mainly by the  $(\text{BiO})_2\text{CO}_3$  phase, showing the characteristic 002, 011, and 013 reflexes at 12.8, 23.9, and 30.3°, respectively (Figure 1a). Thus, annealing in an  $\text{O}_2$ -rich atmosphere stabilizes the bismuth subcarbonate phase at the expense of the chlorinated one. Thermal treatment in air at 420 °C (6 h) led to the formation of nanocomposites rich in  $\text{Bi}_{12}\text{O}_{17}\text{Cl}_2$ , and after a fast annealing at 500 °C (1 h, steep heating),  $(\text{BiO})_2\text{CO}_3$ -related signals were no longer detectable in the diffraction pattern. Finally, prolonged cold UV treatments (14 h) on as-prepared samples resulted in the formation of nanocomposites with  $(\text{BiO})_2\text{CO}_3$  as the main crystalline phase. In the diffraction pattern of UV samples, the peaks are broader compared to those of all of the other samples, suggesting a lower crystallinity and/or the copresence of tiny crystallites of both  $\text{Bi}_{12}\text{O}_{17}\text{Cl}_2$  and  $(\text{BiO})_2\text{CO}_3$ .

The structural features of the various materials obtained by the different annealing procedures were also observed in the Raman spectra (Figure 2). For the UV-treated sample we observed a

simple spectrum characterized by a single peak at  $163\text{ cm}^{-1}$  closely matching that of commercial  $(\text{BiO})_2\text{CO}_3$ . The band is associated with external vibration modes of  $(\text{BiO})_2\text{CO}_3$ ,<sup>45,49</sup> which is the predominant crystal phase in these samples, as indicated by XRD. Moreover, the broad peak shape, already observed in the XRD pattern, suggests the presence of structural disorder. In all thermally treated specimens, additional Raman signals at 96, 474, and  $600\text{ cm}^{-1}$ , attributed to  $\text{Bi}_{12}\text{O}_{17}\text{Cl}_2$ , were also detected.

These findings are confirmed by the analysis of the low-frequency region of the Raman spectra. Indeed, only the peaks related to the  $\text{Bi}_{12}\text{O}_{17}\text{Cl}_2$  phase occur below  $40\text{ cm}^{-1}$ , and we clearly observe them at ca. 9, 20, and  $33\text{ cm}^{-1}$ . Compared with XRD patterns, which show many overlapped signals, Raman spectra are simpler and provide a more precise representation of the system evolution. The observed variations are due to differences in composition and the overall spectral shape derives from the overlap of the spectra of the pure components weighted for their amount. We determined the relative phase composition in the different samples by evaluating (eq 1) the ratio between the integrated area of peaks at 96 and  $163\text{ cm}^{-1}$ , belonging to  $\text{Bi}_{12}\text{O}_{17}\text{Cl}_2$  and  $(\text{BiO})_2\text{CO}_3$ , respectively. In this way, we estimated the effect of the different treatments on the relative amount of  $\text{Bi}_{12}\text{O}_{17}\text{Cl}_2/(\text{BiO})_2\text{CO}_3$  (Figure 3).

We found that the ratio between  $\text{Bi}_{12}\text{O}_{17}\text{Cl}_2$  and  $(\text{BiO})_2\text{CO}_3$  is ca. 1 for AP and T42 samples. At variance, after the fast annealing at 500 °C, the relative composition is 100%  $\text{Bi}_{12}\text{O}_{17}\text{Cl}_2$  (Figure 3), which turns to 100%  $(\text{BiO})_2\text{CO}_3$  after prolonged cold UV treatment. These findings highlight that the selected annealing procedures allow us to modulate the sample composition in a wide range.

The capability of the employed UV procedure to produce materials containing high amounts of  $(\text{BiO})_2\text{CO}_3$  can be rationalized taking into account the nature of the treatment. Basically, it is a photocatalytic reaction promoted by UV light that leads to the decomposition of surfactant molecules. Among all of the possible decomposition species of organic compounds, carbon dioxide is usually formed, and it is likely that the bismuth

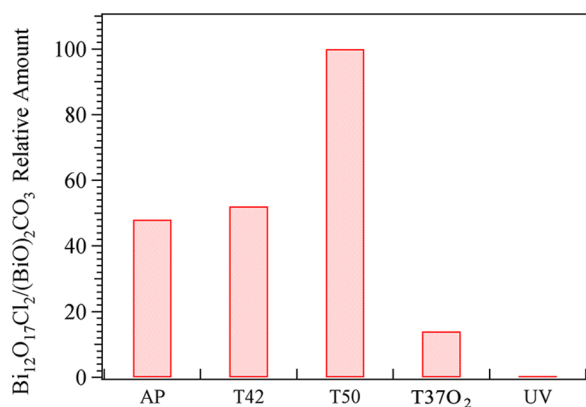


**Figure 3.** Relative composition of Bi<sub>12</sub>O<sub>17</sub>Cl<sub>2</sub>/(BiO)<sub>2</sub>CO<sub>3</sub> nanocomposite materials subjected to different treatments determined from Raman spectra (eq 1).

subcarbonate phase is obtained by reaction of CO<sub>2</sub> with the inorganic matrix. Moreover, because the UV treatments were conducted on aqueous dispersions of the samples, the presence of water hampers the removal of CO<sub>2</sub> from the catalyst and promotes the formation of HCO<sub>3</sub><sup>-</sup> and CO<sub>3</sub><sup>2-</sup> species. At variance, short thermal treatments (1 h) at 500 °C and steep heating/cooling steps allow the fast removal of the surfactant pyrolysis products from the reaction environment, thus favoring the formation of inorganic compounds free from carbon-containing phases.

Specific surface area (SSA) and sample morphologies are important parameters being directly related to the adsorption capability. All samples showed surface area values up to few tenths of square meters per gram of catalyst, which are typical values for BiO<sup>+</sup>-based materials<sup>29,40,41,50</sup> (Table 1). In particular, the UV sample reaches the highest values, 21 m<sup>2</sup> g<sup>-1</sup>, whereas commercial (BiO)<sub>2</sub>CO<sub>3</sub> shows a SSA value 1 order of magnitude lower.

**Table 1.** Specific Surface Area Values of Bi<sub>12</sub>O<sub>17</sub>Cl<sub>2</sub>/(BiO)<sub>2</sub>CO<sub>3</sub> Nanocomposite Materials

sample	SSA (m <sup>2</sup> g <sup>-1</sup> )
T50	16
T42	6
T37O <sub>2</sub>	11
UV	21
(BiO) <sub>2</sub> CO <sub>3</sub>	2

Different morphologies were observed especially by employing the fast treatment at 500 °C and UV radiation. As shown in Figure 4a,b, AP samples were characterized by the presence of randomly oriented aggregates of irregular shape, constituted by very thin flakes, few nanometers thick and hundreds of nanometers wide.

By applying thermal treatments at increasing temperature, up to 420 °C, substantial differences from as-prepared samples were not observed. Instead, for the T50 sample (Figure 4c,d), a highly homogeneous distribution of very thin flakes of similar dimensions (a hundred of nanometer wide) was observed. Flakes coalescence has not been detected despite the high temperature and the steep heating time. Furthermore, samples subjected to UV light irradiation displayed an even more different morphology, characterized by a spongy texture. In Figure 4e,f, micrometric aggregates constituted by randomly

orientated thin flakes one hundred nanometers wide can be appreciated.

The relative composition of Bi<sub>12</sub>O<sub>17</sub>Cl<sub>2</sub>/(BiO)<sub>2</sub>CO<sub>3</sub> nanocomposite materials is directly correlated with the optical properties, and its modulation allows the tuning of light absorption. In particular, sustainable strategies in environmental remediation require materials that absorb in the visible range to exploit solar radiation. In this regard, samples characterized by high amounts of Bi<sub>12</sub>O<sub>17</sub>Cl<sub>2</sub> presented a high absorption in the visible range (Figure 5), which instead decreased when the subcarbonate phase was predominant. Indeed, Bi<sub>12</sub>O<sub>17</sub>Cl<sub>2</sub> and (BiO)<sub>2</sub>CO<sub>3</sub> are characterized by absorption edges localized around 520 and 400 nm, respectively.<sup>51–53</sup> Interestingly, the UV sample for which chlorinated phases were not detected (Figures 1a and 2) shows an absorption spectrum characterized by a long tail in the visible range. A similar feature, usually not observable in the spectra of pure and single-phase (BiO)<sub>2</sub>CO<sub>3</sub>, is attributed to the presence of defects and low- or noncrystalline materials not detectable with XRD and Raman spectroscopy.

In adsorption–degradation processes, the material surface plays a paramount role. In this regard, X-ray photoelectron spectroscopy gives qualitative and quantitative information on the species present on the sample surface.

The survey spectra of all samples showed Bi, O, Cl, and C characteristic peaks (in Figure 6a, the AP sample is reported). The Bi4f high-resolution spectrum (inset Figure 6a) displayed two intense peaks at binding energy (BE) = 159.0 and 164.3 eV, which can be assigned to the *j* = 7/2 and 5/2 components of bismuth in the +3 oxidation state.<sup>54,55</sup>

On the surface of both UV and T50 samples, carbonate- and Cl<sup>-</sup>-related signals were observed by XPS, evidencing the copresence of bismuth subcarbonate- and oxychloride-related species not detected by XRD and Raman spectroscopy (Figures 1a and 2). In this regard, it is noteworthy that XRD is sensitive only to crystalline materials and the features of Raman spectra, that is, peak intensity and width, strongly depend on sample crystallinity. Concerning UV samples, chlorine-containing species observed by XPS contributed to the shape of the Bi<sub>12</sub>O<sub>17</sub>Cl<sub>2</sub>/(BiO)<sub>2</sub>CO<sub>3</sub> nanocomposite absorption spectrum characterized by a shoulder in the visible range (*λ* > 400 nm, Figure 5).

The presence of carbonates is confirmed by C1s high-resolution spectra. Moreover, the carbon signal gives clear indication of the annealing treatment effectiveness on the achievement of a pure inorganic material. In particular, the C1s photoelectron peak of AP samples showed a broad profile due to the presence of multiple species. This is not surprising because, as previously discussed (Figure 1), crude samples still contain surfactant molecules. The component at a lower BE (I, Figure 6b) can be assigned to adventitious carbon (BE = 284.8 eV) and to the aliphatic residues of the surfactant.<sup>54,56</sup> The two components centered at 286.7 and 288.7 eV are, respectively, ascribed to ether groups (II, Figure 6b) of the residual surfactant and to carbonate groups (III, Figure 6b). In fact, the employed highly alkaline synthesis conditions can favor carbonation of the solution through reaction with atmospheric CO<sub>2</sub>. At variance, after thermal and UV light treatments, the efficient removal of the residual surfactant was achieved as pointed out by the disappearance of the signals related to the surfactant moiety (Figure 6b).

The capability of the nanomaterials to purify dye-containing water, through pollutants' adsorption and their successive degradation with visible light, was evaluated by dispersing the

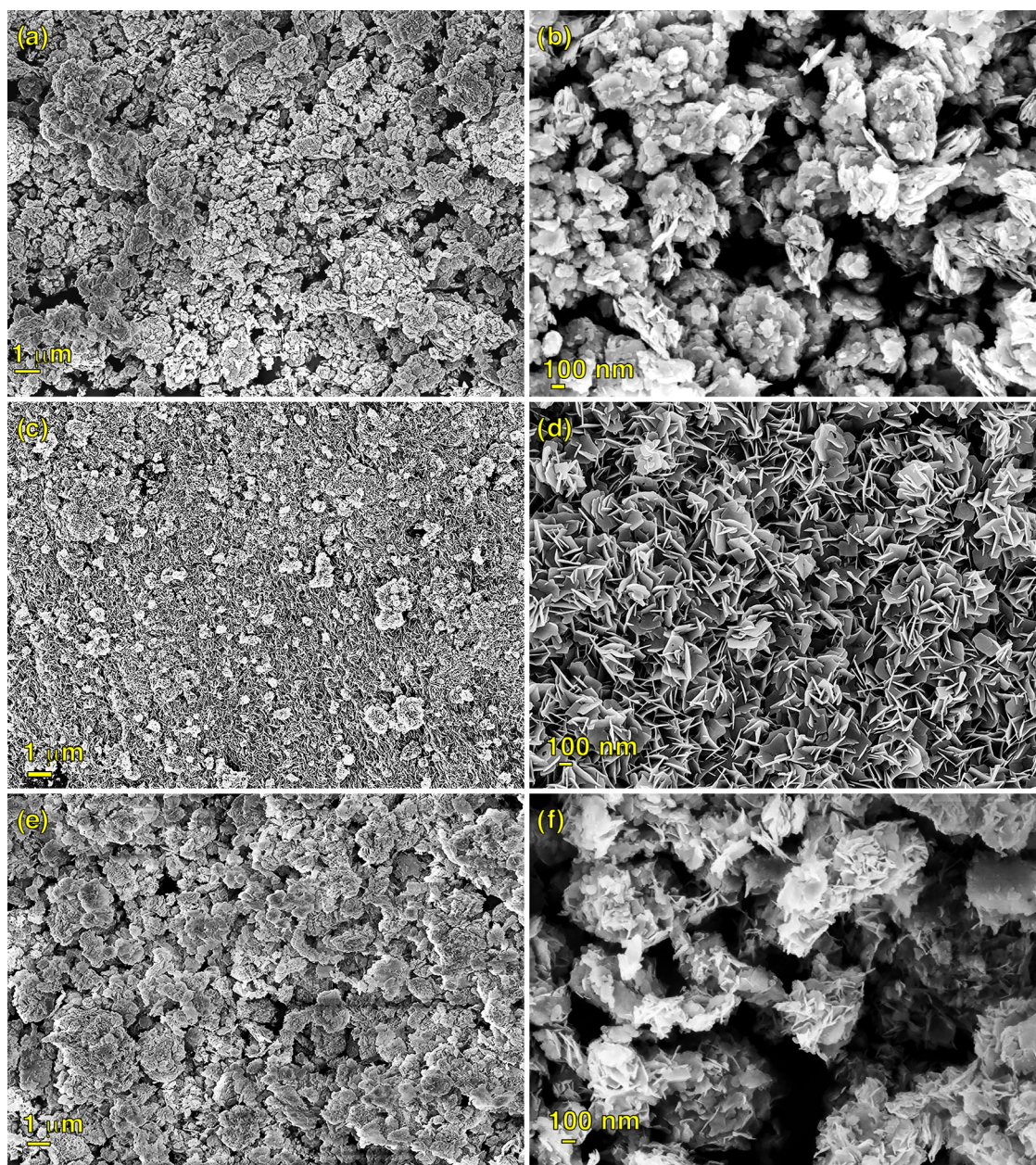


**Figure 4.** SEM images of AP (a, b); T50 (c, d); and UV (e, f) samples.

sample in an aqueous solution containing rhodamine B or methyl orange. Adsorption is a physical process, in which dye molecules are adsorbed on the photocatalyst surface to reach an adsorption–desorption equilibrium before irradiation. Commonly, the adsorption of dye molecules on the photocatalyst surface is a precondition for the degradation reaction. We performed the adsorption–decomposition experiments on the whole set of samples, but we observed that the activity of T42 and T37O<sub>2</sub> specimens was considerably lower than that of T50 and UV. Besides compositional factors, this behavior is presumably affected also by the low SSA values of T42 and T37O<sub>2</sub> (see Table 1). For this reason, we focused our attention and the following discussion on the samples showing higher SSA values, for example, T50 and UV specimens.

In general, the dye-adsorption process consists of three steps: (i) a fast initial regime that strongly depends on electric attraction between the adsorbate and the clean surface of the adsorbent, (ii)

a slow step that can last from several minutes up to 1 h and depends on both electrostatic attraction between the adsorbate and the partially covered surface and the reorganization of the adsorbed molecules, and (iii) achievement of the adsorption/desorption equilibrium.<sup>57,58</sup>

Figure 7 shows the dye-adsorption kinetics in the dark normalized for the material surface area for UV and T50 samples. In both cases, the adsorption process is rather fast and almost complete after the first 10 min, pointing out the effectiveness of these materials to quickly eliminate the pollutants from the solution. The solution fading due to dye adsorption is visible also to the naked eye, as evidenced in the pictures reported in Figure 7. UV samples are more effective in adsorbing both the dyes. Moreover, the results indicate that T50 exhibits a slightly higher adsorption of the anionic MO with respect to that of the cationic RhB, whereas the differences for UV are significantly higher.

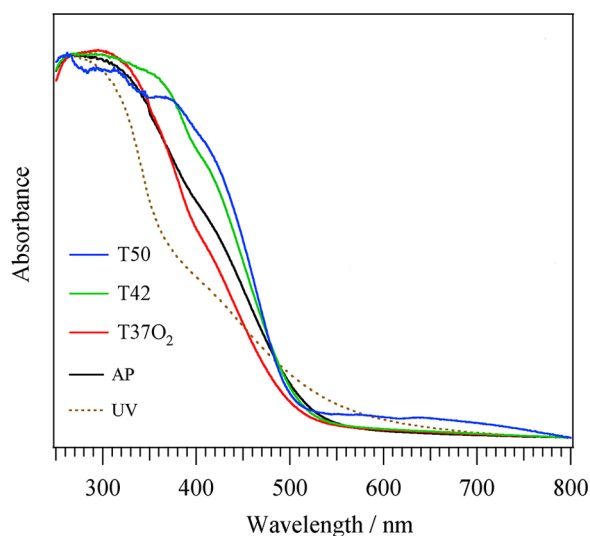


**Figure 5.** UV–vis diffuse reflectance spectra of as-prepared and treated  $\text{Bi}_{12}\text{O}_{17}\text{Cl}_2/(\text{BiO})_2\text{CO}_3$  nanocomposite materials.

The observed adsorption behavior can be interpreted considering the values of  $\zeta$ -potential for T50 (+27 mV) and UV (−12 mV), respectively. In particular,  $\zeta$ -potentials of opposite charges can induce different material–dye interactions.

MO is negatively charged at the working pH and contains an azo group (−N=N−) that links the aromatic C-atoms and hence it is easily adsorbed on the positively charged surface (T50). Conversely, RhB is a cationic dye containing a carboxyl group that under the adopted reaction conditions can be partially present in its basic form and therefore it is able to interact in the zwitterionic form with the surface of T50.

The higher adsorption of MO on UV samples may be partially related to specific surface features. In particular, the negative  $\zeta$ -potential could be associated with the presence of  $\text{OH}^-$  groups adsorbed on the material surface.<sup>59,60</sup> Therefore, the anionic MO molecules can be effectively adsorbed by UV samples by the ligand exchange reaction with the surface-adsorbed  $\text{OH}^-$  groups.<sup>29</sup>

The photocatalytic activity of the different materials was evaluated in solution toward the decoloration of RhB and MO,

under irradiation with visible light. According to literature conditions,<sup>61,62</sup> because of the degradation resistance of MO, the amount of the photocatalyst used was higher than that in the case of RhB. For adsorption studies, the photoactivity was evaluated on the most promising materials and compared to that of commercial  $(\text{BiO})_2\text{CO}_3$ .

In Figure 8, the adsorption capacity (AC, calculated according to eq 2) and the decoloration efficiency (DE, calculated according to eq 3) for RhB are reported. The UV-treated samples have both the highest AC and DE. In fact, they are able to adsorb more than  $6 \text{ mg g}^{-1}$  RhB (Figure 8a), whereas the reference sample and T50 do not reach an AC value of  $5 \text{ mg g}^{-1}$ . For the thermally treated sample, RhB adsorption of ca. 20% (Figure 8b) was observed after the equilibrium was reached between the dye and the adsorbent in the dark (45 min). Then, under irradiation with visible light, another 40% of the organic dye is degraded with a slow but steady rate. After 180 min of reaction, a total decoloration efficiency of 60% was achieved. The UV sample, consisting of a subcarbonate-rich  $\text{Bi}_{12}\text{O}_{17}\text{Cl}_2/(\text{BiO})_2\text{CO}_3$  nanocomposite, showed a much stronger dye adsorption up to 50% (Figure 8b) in the first 45 min. Subsequently, after 180 min of irradiation, it was able to decolorize all of the remaining RhB present in the solution.

Taking into account the absorption spectra of the different samples at  $\lambda > 400 \text{ nm}$  (Figure 5), it is reasonable to suppose that the photodegradation activity toward RhB, under visible irradiation, consists mainly in a combination between (i) indirect photosensitization of the catalyst through the dye and (ii) direct photoexcitation of the catalyst. The balance between these two processes is governed by the relative amount of  $\text{Bi}_{12}\text{O}_{17}\text{Cl}_2$  in the  $\text{Bi}_{12}\text{O}_{17}\text{Cl}_2/(\text{BiO})_2\text{CO}_3$  nanocomposite materials because it has the higher visible light absorption.

The adsorption capacity of the UV samples toward MO (Figure 9a) is more than 3 times larger than that of the other two materials and reaches the value of  $4.3 \text{ mg g}^{-1}$ . At equilibrium, about 80% of MO was adsorbed from the solution, and after 60 min of irradiation, only 3.5% of MO was still present in the solution. The T50 sample showed a lower MO-adsorption capacity (25%), but it was able to degrade around 55% of MO in 180 min (total DE 80%). Instead, the commercial  $(\text{BiO})_2\text{CO}_3$  is almost inactive.

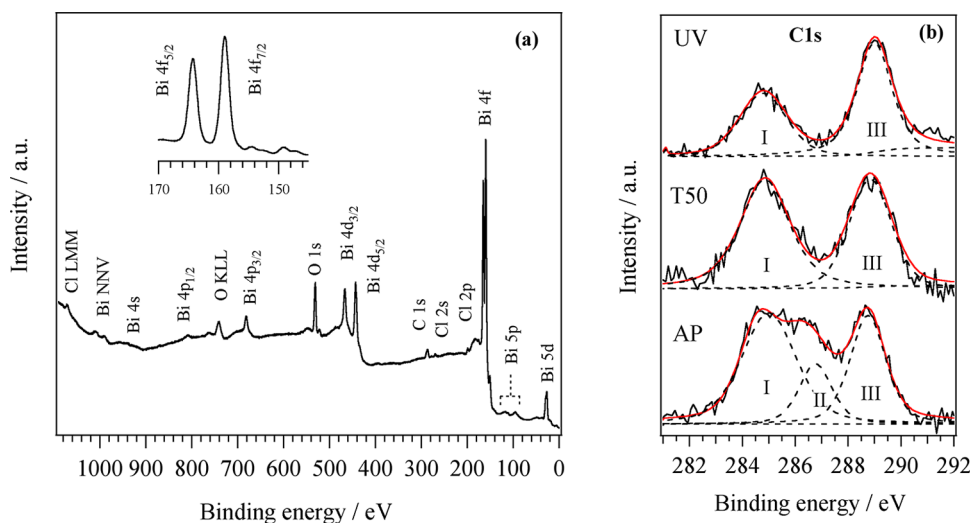


**Figure 6.** XPS spectra: (a) wide scan (survey) and high-resolution Bi4f peak (inset); (b) C1s high-resolution spectra of the AP, T50, and UV samples.

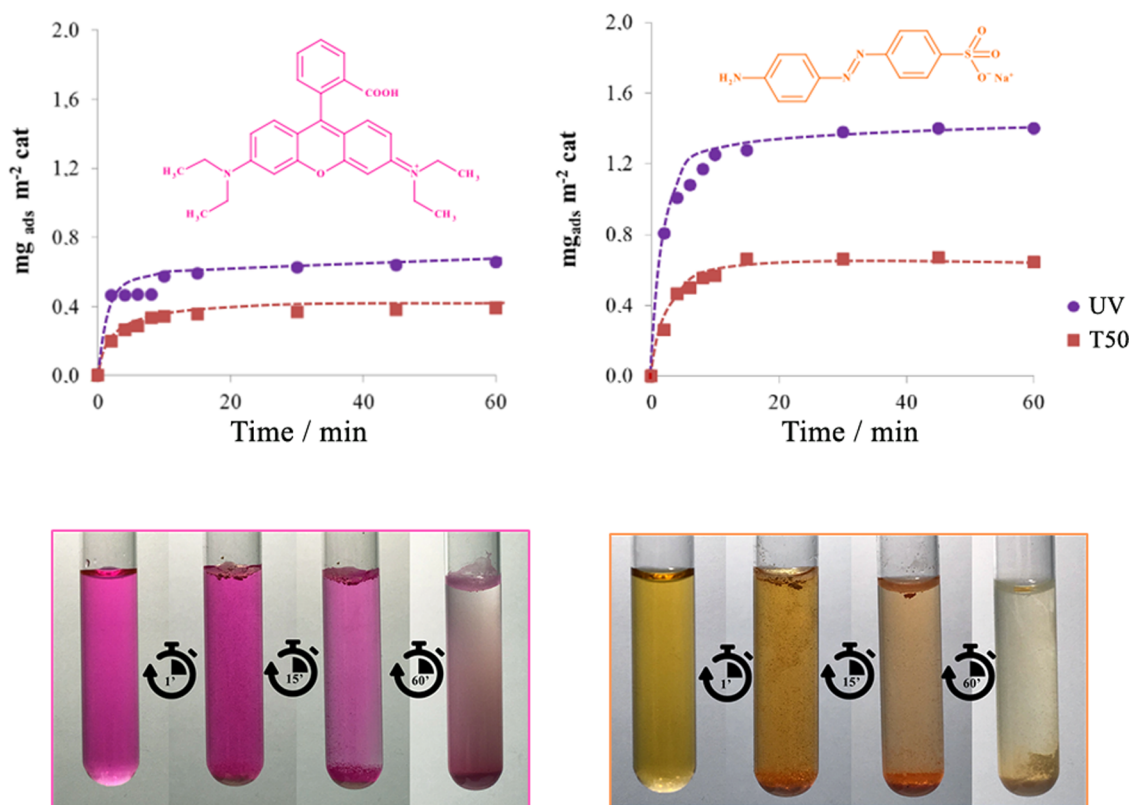


**Figure 7.** Time dependence of the adsorption of RhB and MO over T50 and UV samples in the dark. The pictures illustrate the solution fading due to dye adsorption.

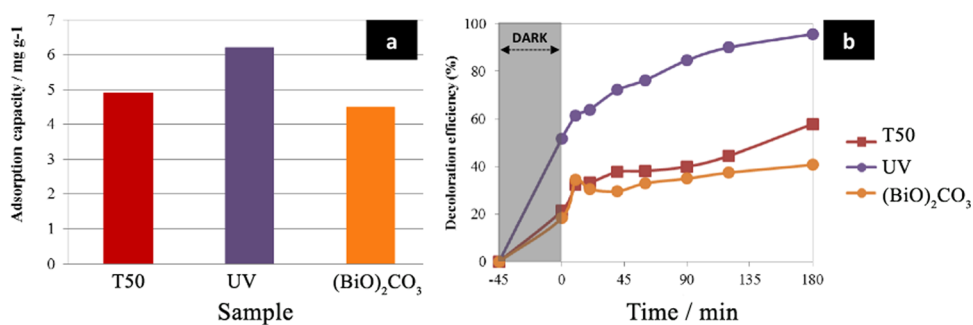


**Figure 8.** a) Adsorption capacity of the T50 and UV samples and commercial (BiO)<sub>2</sub>CO<sub>3</sub> in the presence of RhB. (b) Photocatalytic activity of the samples toward the decoloration efficiency of rhodamine B.

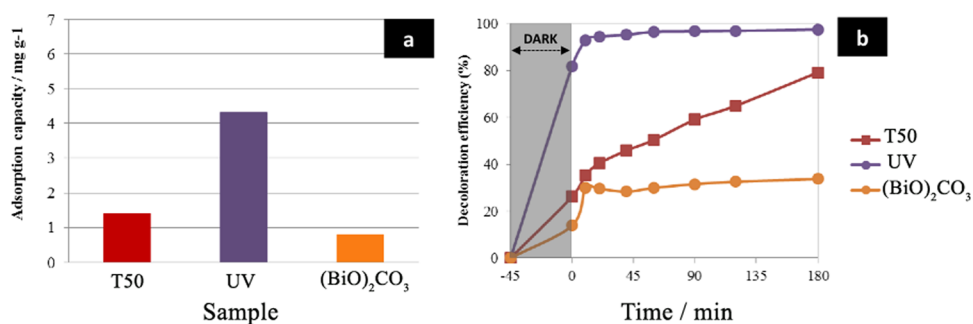
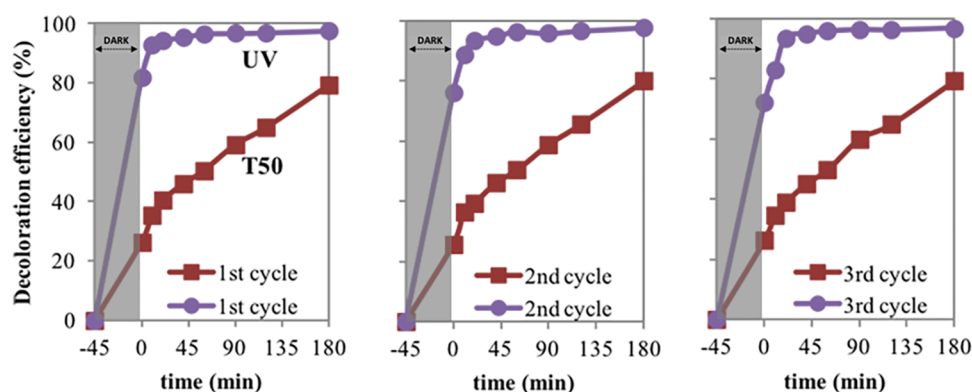


**Figure 9.** a) Adsorption capacity of different samples in the presence of MO. (b) Photocatalytic activity of the samples toward the decoloration of methyl orange.

To determine the stability and recyclability of the catalysts, we performed a set of cyclic tests using the same samples in successive runs. The decoloration efficiency curves (Figure 10)

did not show noticeable variations after each of the three cycles, evidencing a stable photocatalytic activity for both UV and T50 samples.

## Methyl Orange



## Rhodamine B

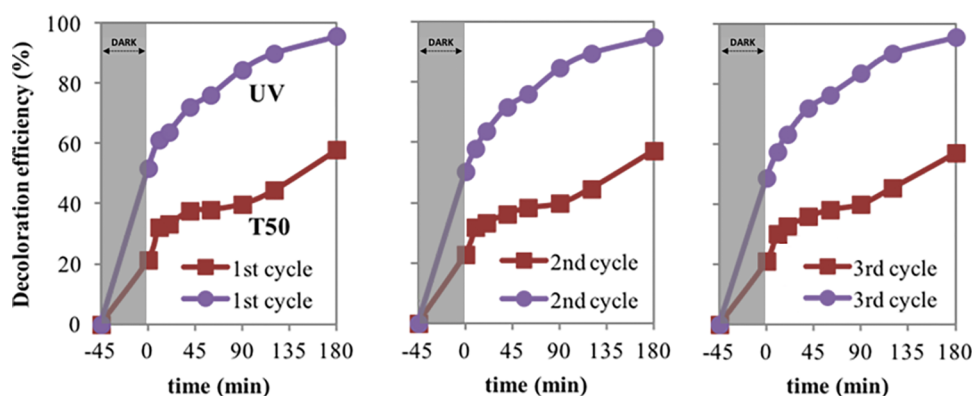


**Figure 10.** Decoloration efficiency in recyclic tests for the photocatalytic reaction of T50 and UV samples toward MO and RhB.

In summary, UV samples represent promising bifunctional materials because they combine fast and significant dye-adsorption capacity with the ability to photodegrade the dyes under visible irradiation. Moreover, they perform very well with both anionic and cationic molecules. In particular, the cold UV light treatment allows us to preserve a reasonably high surface area and a suitable morphology and surface composition that guarantee a better adsorbent behavior compared to that of the thermally treated samples. Nonetheless, the T50 sample, despite its lower adsorption capacity, can also be considered as an interesting bifunctional material, especially toward MO. In fact, the weaker MO-adsorption capability is compensated by a significant photodegradation activity.

### CONCLUSIONS

This study shows that postsynthesis treatments represent a powerful tool for the modulation of the chemophysical and functional properties of  $\text{Bi}_{12}\text{O}_{17}\text{Cl}_2/(\text{BiO})_2\text{CO}_3$  nanocomposite materials obtained by soft solution procedures. Accordingly, a variation of their performances as adsorbents and photocatalysts toward selected cationic (RhB) and anionic (MO) organic dyes can be achieved. Fast treatments at high temperature (up to 500 °C) favor the formation of the  $\text{Bi}_{12}\text{O}_{17}\text{Cl}_2$ -rich nanocomposite, whereas the  $(\text{BiO})_2\text{CO}_3$ -rich nanocomposites were obtained after UV light irradiation. The latter displayed the most promising functional performances with an adsorption capacity

of 6.0 and 4.3  $\text{mg g}^{-1}$  in 60 min toward RhB and MO, respectively. The majority of the adsorption (80%) occurs within the first 10 min of contact with the dyes. Interestingly, thanks to their visible-light-driven photocatalytic activity UV samples were also able to contribute to degradation of RhB. The increased content of  $\text{Bi}_{12}\text{O}_{17}\text{Cl}_2$  in the  $\text{Bi}_{12}\text{O}_{17}\text{Cl}_2/(\text{BiO})_2\text{CO}_3$  nanocomposite materials slightly reduced the adsorption performance toward RhB (5  $\text{mg g}^{-1}$ ), whereas it significantly affects the MO-adsorption capacity (1.5  $\text{mg g}^{-1}$ ). However, thanks to the stronger absorption in the visible range  $\text{Bi}_{12}\text{O}_{17}\text{Cl}_2$ -rich composite materials are more efficient photocatalysts.

The obtained results evidenced the ability of the employed strategy to modulate sample properties in a wide range, thus pointing out the effectiveness of this approach for the synthesis of multifunctional inorganic materials for environmental remediation. In particular, among the different adopted procedures, cold treatment with UV light on crude  $\text{Bi}_{12}\text{O}_{17}\text{Cl}_2/(\text{BiO})_2\text{CO}_3$  nanocomposites guarantees relatively fast and high dye-adsorption capacity and maintains photocatalytic degradation activity under sustainable visible light conditions even after successive working cycles.

### EXPERIMENTAL SECTION

**Synthesis.** All chemicals were purchased from Sigma-Aldrich and used as received. Syntheses were conducted under mild conditions in aqueous solution in the presence of Brij 76 as a

surfactant. Solution A was obtained by dissolving BiCl<sub>3</sub> (0.2 M) in a HCl/ethanol solution (0.5 M) at room temperature, whereas solution B was prepared by mixing Brij 76 (1 wt %) and HCl (0.6 M) at 65 °C. Solution A was added to solution B (volume ratio 1:15), and the resulting mixture was aged 5 h at 65 °C under continuous and vigorous stirring. The raw powders were precipitated with an excess of LiOH (2.0 M), collected by centrifugation, washed with water and ethanol, and finally dried in air. Thermal or cold UV treatments were conducted on the as-prepared samples. In particular, the following annealing procedures were performed: (i) 1 h at 500 °C in air (sample inserted and removed in temperature); (ii) 6 h at 420 °C in air (heating ramp 0.5 °C min<sup>-1</sup>); and (iii) 6 h at 370 °C in O<sub>2</sub> 30% in Ar (heating ramp 0.5 °C min<sup>-1</sup>). UV treatments at room temperature were conducted by dispersing the powders in aqueous solution and irradiating the mixture with a medium-pressure Hg lamp (450 W) for 14 h. To verify the complete removal of surfactant after the UV procedure, temperature-programmed oxidation experiments were conducted after the above-mentioned treatments to check the presence of residual organic contaminants.

Table 2 summarizes the treatments carried out on as-prepared powders and their corresponding sample labels.

**Table 2. Treatment Conditions for Bi<sub>12</sub>O<sub>17</sub>Cl<sub>2</sub>/(BiO)<sub>2</sub>CO<sub>3</sub> Composite Nanomaterials**

sample name	postsynthetic treatment
T50	1 h at 500 °C in air (sample inserted and removed at this temperature)
T42	6 h at 420 °C (heating ramp 0.5 °C min <sup>-1</sup> ), in air
T37O <sub>2</sub>	6 h at 370 °C (heating ramp 0.5 °C min <sup>-1</sup> ), in O <sub>2</sub> (30% in Ar)
UV	irradiating for 14 h by a medium-pressure Hg lamp (450 W)
AP	as-prepared sample
(BiO) <sub>2</sub> CO <sub>3</sub>	commercial sample

**Thermogravimetric Analysis (TGA).** TGA experiments were performed with a TA Instruments SDT 2960 simultaneous thermogravimetric/differential scanning calorimetry system. The scans were recorded in air with a heating rate of 10 °C min<sup>-1</sup> in a temperature range of 30–800 °C.

**X-ray Diffraction (XRD).** XRD spectra were collected with a Bruker D8 Advance diffractometer, in Bragg–Brentano geometry, equipped with a Göbel mirror using Cu K $\alpha$  as a source operating at 40 kV and 40 mA. The patterns were acquired in the 10–70° 2 $\theta$  range (0.03°/step and 10 s/step).

**Raman Spectroscopy.** Micro-Raman experiments were carried out in backscattering geometry at room temperature using an Horiba T64000 triple spectrometer equipped with a Peltier-cooled charge-coupled device detector (Horiba Synapse). The 514.5 nm line of an argon laser (Spectra Physics Stabilite 2017) was used as the excitation source. The laser power at the specimen surface was always kept below 5 mW. Care was taken to avoid sample damage due to the interaction with the laser beam. The scattered radiation was collected through a long working distance 50 $\times$  microscope objective (Olympus LMPLFLN, 50 $\times$ /0.50).

The spectrograph, equipped with 2400 lines/mm gratings, was used in double subtractive configuration for the low-wavenumber-region (5–250 cm<sup>-1</sup>) measurements or as a single stage in the 70–1000 cm<sup>-1</sup> range. The relative amount of Bi<sub>12</sub>O<sub>17</sub>Cl<sub>2</sub> and (BiO)<sub>2</sub>CO<sub>3</sub> was determined by the following equation (eq 1)

$$\text{Bi}_{12}\text{O}_{17}\text{Cl}_2/(\text{BiO})_2\text{CO}_3 (\%) = \frac{R}{R_0} \times 100 \quad (1)$$

where  $R$  is the ratio of the integrated area of peaks at 96 and 163 cm<sup>-1</sup>, characteristics of Bi<sub>12</sub>O<sub>17</sub>Cl<sub>2</sub> and (BiO)<sub>2</sub>CO<sub>3</sub>, respectively, and  $R_0$  is the value of  $R$  for sample T50.

**Absorption Spectroscopy.** Diffuse reflectance spectra in the range 250–800 nm were performed on a CARYSE spectrophotometer equipped with an internal diffuse reflectance accessory consisting of a poly(tetrafluoroethylene)-coated integration sphere. The spectra were acquired in reflectance mode ( $R\%$ ) with a spectral band width of 4 nm and converted to absorbance by means of the Cary WinUV 3.00 software package.

**Scanning Electron Microscopy (SEM).** The morphology of the samples was investigated by field emission SEM analysis. SEM measurements were performed by a Sigma Zeiss instrument operated at an acceleration voltage of 5 kV collecting the secondary electron signal.

**X-ray Photoelectron Spectroscopy (XPS).** XPS measurements were performed on a PerkinElmer  $\Phi$  5600ci spectrometer using a nonmonochromatized Mg K $\alpha$  radiation (1253.6 eV), at a working pressure lower than 10<sup>-9</sup> mbar. The specimens, mounted on steel sample holders, were introduced directly into the XPS analytical chamber by a fast entry lock system. The sample analysis area was 800  $\mu\text{m}$  in diameter. Survey scans were run in the 0–1100 eV range. Detailed spectra were recorded for the following regions: Bi4f, Cl2p, O1s, and C1s. The reported binding energies (BEs, standard deviation  $\pm$  0.2 eV) were corrected for charging effects by assigning to the C1s peak associated with adventitious carbon a BE of 284.8 eV. The analysis involved Shirley-type background subtraction and, whenever necessary, spectral deconvolution, which was carried out by nonlinear least-squares curve fitting, adopting a Gaussian–Lorentzian sum function. The atomic composition of the samples was calculated by peak integration, using sensitivity factors provided by the spectrometer manufacturer ( $\Phi$  V5.4A software) and taking into account the geometric configuration of the apparatus. The experimental uncertainty on the atomic composition values does not exceed  $\pm 5\%$ .

**Specific Surface Area and  $\zeta$  Potential.** Specific surface area values were obtained from Brunauer, Emmett, and Teller analysis of krypton adsorption isotherms at liquid nitrogen temperature (ASAP 2020; Micromeritics). Before analysis, the samples were degassed at 120 °C for 12 h.

$\zeta$  Potential measurements were performed on a catalyst dispersion (1 mg mL<sup>-1</sup>) in Milli-Q water using a zetasizer NanoZS (Malvern Instruments Ltd., U.K.). The analyses were performed in triplicate at 20 °C.

**Adsorption Kinetic Experiment.** The material (100 mg) was dispersed in 160 mL of an aqueous RhB or MO solution with an initial concentration ( $C_0$ ) of 6 mg L<sup>-1</sup>, and the suspension was magnetically stirred in the dark. The suspension temperature was maintained at 20 °C. At given time intervals, 3 mL aliquots were sampled and filtered through a 0.45  $\mu\text{m}$  Millipore filter to remove the catalyst. The concentration of dyes in the filtrates was evaluated by recording the absorbance at the maximum of the absorption spectrum of the target molecule (554 nm for RhB, 464 nm for MO) by means of a UV–vis spectrometer (Shimadzu UV-2450).

The material adsorption capacity (AC) was calculated from the following equation

$$AC \text{ (mg g}^{-1}\text{)} = \frac{(C_0 - C_{eq})V}{m} \quad (2)$$

where  $C_0$  and  $C_{eq}$  ( $\text{mg L}^{-1}$ ) are the concentrations of the dye solution at the initial stage and at the instant  $t_{eq} = 45$  min when the adsorption–desorption equilibrium is reached,  $m$  (g) is the mass of the sample, and  $V$  (L) is the volume of the adsorbate solution.

**Photocatalytic Experiments.** Photocatalytic properties of the samples were investigated by monitoring the decoloration of organic dye aqueous solution under visible light. RhB and MO were used as models of cationic and anionic pollutants, respectively. The description of the experimental setup is discussed in detail elsewhere.<sup>63</sup> In a typical experiment with MO, 200 mg of the catalyst was dispersed in a dye aqueous solution ( $6 \text{ mg L}^{-1}$ ,  $1.9 \times 10^{-5} \text{ M}$ ). In the case of RhB, 50 mg of the catalyst and  $1.5 \times 10^{-5} \text{ M}$  dye solution ( $6 \text{ mg L}^{-1}$ ) were used. Prior to irradiation, the dye/catalyst suspensions were kept in dark for 45 min under stirring to ensure the achievement of the adsorption–desorption equilibrium under ambient conditions. During irradiation, at increasing time intervals, aliquots of the suspension were withdrawn and filtered through a  $0.45 \mu\text{m}$  Millipore filter to remove the catalyst. The residual dye concentrations in the filtrates were analyzed by a UV–visible spectrophotometer (Shimadzu UV-2450) at maximum absorption wavelengths ( $\lambda_{\text{max}}$ ) of 554 and 464 nm for RhB and MO, respectively.

The decoloration efficiency (DE) was calculated from the following equation

$$DE \text{ (\%)} = \frac{(C_0 - C_t)}{C_0} \times 100 \quad (3)$$

where  $C_0$  and  $C_t$  ( $\text{mg L}^{-1}$ ) are the concentrations of the dye solution at the initial stage and at the  $t$  instant ( $45 < t < 180$  min), respectively.

## AUTHOR INFORMATION

### Corresponding Authors

\*E-mail: gregorio.bottaro@cnr.it (G.B.)

\*E-mail: vgombac@units.it (V.G.).

### ORCID

Gregorio Bottaro: 0000-0001-6196-8638

Paolo Fornasiero: 0000-0003-1082-9157

### Notes

The authors declare no competing financial interest.

## ACKNOWLEDGMENTS

The authors gratefully acknowledge Dr. Roberta Saini for TGA analysis and Drs. Monica Fabrizio and Simone Battiston for SEM images.

## REFERENCES

- Forgacs, E.; Cserháti, T.; Oros, G. Removal of synthetic dyes from wastewaters: a review. *Environ. Int.* **2004**, *30*, 953.
- Bae, J.-S.; Freeman, H. S. Aquatic toxicity evaluation of new direct dyes to the *Daphnia magna*. *Dyes Pigm.* **2007**, *73*, 81.
- Combes, R. D.; Haveland-Smith, R. B. A review of the genotoxicity of food, drug and cosmetic colours and other azo, triphenylmethane and xanthene dyes. *Mutat. Res., Rev. Genet. Toxicol.* **1982**, *98*, 101.
- Hatch, K. L.; Maibach, H. Dyes as contact allergens: A comprehensive record. *Text. Chem. Color. Am. Dyest. Rep.* **1999**, *1*, 53.
- Rai, H. S.; Bhattacharyya, M. S.; Singh, J.; Bansal, T. K.; Vats, P.; Banerjee, U. C. Removal of Dyes from the Effluent of Textile and

Dyestuff Manufacturing Industry: A Review of Emerging Techniques With Reference to Biological Treatment. *Crit. Rev. Environ. Sci. Technol.* **2005**, *35*, 219.

(6) Kuo, W. G. Decolorizing dye wastewater with Fenton's reagent. *Water Res.* **1992**, *26*, 881.

(7) Walsh, G. E.; Bahner, L. H.; Horning, W. B. Toxicity of textile mill effluents to freshwater and estuarine algae, crustaceans and fishes. *Environ. Pollut., Ser. A* **1980**, *21*, 169.

(8) Karunya, A.; Rose, C.; Nachiyar, C. V. Biodegradation of the textile dye Mordant Black 17 (Calcon) by *Moraxella osloensis* isolated from textile effluent-contaminated site. *World J. Microbiol. Biotechnol.* **2014**, *30*, 915.

(9) Cheng, L.; Wei, M.; Huang, L.; Pan, F.; Xia, D.; Li, X.; Xu, A. Efficient  $\text{H}_2\text{O}_2$  Oxidation of Organic Dyes Catalyzed by Simple Copper(II) Ions in Bicarbonate Aqueous Solution. *Ind. Eng. Chem. Res.* **2014**, *53*, 3478.

(10) Morshedi, D.; Mohammadi, Z.; Boojar, M. M. A.; Aliakbari, F. Using protein nanofibrils to remove azo dyes from aqueous solution by the coagulation process. *Colloids Surf., B* **2013**, *112*, 245.

(11) Zheng, Y.; Yao, G.; Cheng, Q.; Yu, S.; Liu, M.; Gao, C. Positively charged thin-film composite hollow fiber nanofiltration membrane for the removal of cationic dyes through submerged filtration. *Desalination* **2013**, *328*, 42.

(12) You, S.-J.; Damodar, R. A.; Hou, S.-C. Degradation of Reactive Black 5 dye using anaerobic/aerobic membrane bioreactor (MBR) and photochemical membrane reactor. *J. Hazard. Mater.* **2010**, *177*, 1112.

(13) Yue, Q. Y.; Gao, B. Y.; Wang, Y.; Zhang, H.; Sun, X.; Wang, S. G.; Gu, R. R. Synthesis of polyamine flocculants and their potential use in treating dye wastewater. *J. Hazard. Mater.* **2008**, *152*, 221.

(14) Raghu, S.; Basha, C. A. Chemical or electrochemical techniques, followed by ion exchange, for recycle of textile dye wastewater. *J. Hazard. Mater.* **2007**, *149*, 324.

(15) Belessi, V.; Romanos, G.; Boukos, N.; Lambropoulou, D.; Trapalis, C. Removal of Reactive Red 195 from aqueous solutions by adsorption on the surface of  $\text{TiO}_2$  nanoparticles. *J. Hazard. Mater.* **2009**, *170*, 836.

(16) Gupta, V. K.; Suhas. Application of low-cost adsorbents for dye removal – A review. *J. Environ. Manage.* **2009**, *90*, 2313.

(17) Asuha, S.; Zhou, X. G.; Zhao, S. Adsorption of methyl orange and Cr(VI) on mesoporous  $\text{TiO}_2$  prepared by hydrothermal method. *J. Hazard. Mater.* **2010**, *181*, 204.

(18) Wu, R.; Qu, J.; He, H.; Yu, Y. Removal of azo-dye Acid Red B (ARB) by adsorption and catalytic combustion using magnetic  $\text{CuFe}_2\text{O}_4$  powder. *Appl. Catal., B* **2004**, *48*, 49.

(19) Wu, R.; Qu, J.; Chen, Y. Magnetic powder  $\text{MnO-Fe}_2\text{O}_3$  composite—a novel material for the removal of azo-dye from water. *Water Res.* **2005**, *39*, 630.

(20) Park, H.; Kim, H.-i.; Moon, G.-h.; Choi, W. Photoinduced charge transfer processes in solar photocatalysis based on modified  $\text{TiO}_2$ . *Energy Environ. Sci.* **2016**, *9*, 411.

(21) Chang, X.; Wang, S.; Qi, Q.; Gondal, M. A.; Rashid, S. G.; Yang, D.; Dastageer, M. A.; Shen, K.; Xu, Q.; Wang, P. Constrained growth of ultrasmall  $\text{BiOCl}$  nanodiscs with a low percentage of exposed  $\{001\}$  facets and their enhanced photoreactivity under visible light irradiation. *Appl. Catal., B* **2015**, *176–177*, 201.

(22) Li, H.; Shang, J.; Ai, Z.; Zhang, L. Efficient Visible Light Nitrogen Fixation with  $\text{BiOBr}$  Nanosheets of Oxygen Vacancies on the Exposed  $\{001\}$  Facets. *J. Am. Chem. Soc.* **2015**, *137*, 6393.

(23) Ye, L.; Su, Y.; Jin, X.; Xie, H.; Zhang, C. Recent advances in  $\text{BiOX}$  ( $X = \text{Cl, Br and I}$ ) photocatalysts: synthesis, modification, facet effects and mechanisms. *Environ. Sci.: Nano* **2014**, *1*, 90.

(24) Wang, W.-K.; Chen, J.-J.; Gao, M.; Huang, Y.-X.; Zhang, X.; Yu, H.-Q. Photocatalytic degradation of atrazine by boron-doped  $\text{TiO}_2$  with a tunable rutile/anatase ratio. *Appl. Catal., B* **2016**, *195*, 69.

(25) Pei, D.-N.; Gong, L.; Zhang, A.-Y.; Zhang, X.; Chen, J.-J.; Mu, Y.; Yu, H.-Q. Defective titanium dioxide single crystals exposed by high-energy  $\{001\}$  facets for efficient oxygen reduction. *Nat. Commun.* **2015**, *6*, No. 8696.

- (26) Liu, C.; Zhang, A.-Y.; Pei, D.-N.; Yu, H.-Q. Efficient Electrochemical Reduction of Nitrobenzene by Defect-Engineered  $\text{TiO}_{2-x}$  Single Crystals. *Environ. Sci. Technol.* **2016**, *50*, 5234.
- (27) Yu, Y.; Hu, Z.; Zhang, Y.; Gao, H. CTAB@BiOCl: a highly adsorptive photocatalyst for eliminating dye contamination. *RSC Adv.* **2016**, *6*, 18577.
- (28) He, J.; Wang, J.; Liu, Y.; Mirza, Z. A.; Zhao, C.; Xiao, W. Microwave-assisted synthesis of BiOCl and its adsorption and photocatalytic activity. *Ceram. Int.* **2015**, *41*, 8028.
- (29) Selvamani, T.; Raj, B. G. S.; Anandan, S.; Wu, J. J.; Ashokkumar, M. Synthesis of morphology-controlled bismutite for selective applications. *Phys. Chem. Chem. Phys.* **2016**, *18*, 7768.
- (30) Kim, W. J.; Pradhan, D.; Min, B.-K.; Sohn, Y. Adsorption/photocatalytic activity and fundamental natures of BiOCl and  $\text{BiOCl}_{1-x}$ , prepared in water and ethylene glycol environments, and Ag and Au-doping effects. *Appl. Catal., B* **2014**, *147*, 711.
- (31) Xiong, M.; Chen, L.; Yuan, Q.; He, J.; Luo, S.-L.; Au, C.-T.; Yin, S.-F. Facile fabrication and enhanced photosensitized degradation performance of the  $\text{g-C}_3\text{N}_4\text{-Bi}_2\text{O}_2\text{CO}_3$  composite. *Dalton Trans.* **2014**, *43*, 8331.
- (32) Peng, Y.; Wang, K. K.; Yu, P.-P.; Liu, T.; Xu, A. W. Synthesis of one-dimensional  $\text{Bi}_2\text{O}_2\text{CO}_3\text{-Bi}(\text{OHC}_2\text{O}_4)\cdot 2\text{H}_2\text{O}$  heterojunctions with excellent adsorptive and photocatalytic performance. *RSC Adv.* **2016**, *6*, 42452.
- (33) Madhusudan, P.; Zhang, J.; Cheng, B.; Liu, G. Photocatalytic degradation of organic dyes with hierarchical  $\text{Bi}_2\text{O}_2\text{CO}_3$  microstructures under visible-light. *CrystEngComm* **2013**, *15*, 231.
- (34) Chen, L.; Yin, S.-F.; Luo, S.-L.; Huang, R.; Zhang, Q.; Hong, T.; Au, P. C. T.  $\text{Bi}_2\text{O}_2\text{CO}_3/\text{BiOI}$  Photocatalysts with Heterojunctions Highly Efficient for Visible-Light Treatment of Dye-Containing Wastewater. *Ind. Eng. Chem. Res.* **2012**, *51*, 6760.
- (35) Chen, L.; Huang, R.; Yin, S.-F.; Luo, S.-L.; Au, C.-T. Flower-like  $\text{Bi}_2\text{O}_2\text{CO}_3$ : Facile synthesis and their photocatalytic application in treatment of dye-containing wastewater. *Chem. Eng. J.* **2012**, *193–194*, 123.
- (36) Wang, C.-Y.; Zhang, X.; Qiu, H.-B.; Wang, W.-K.; Huang, G.-X.; Jiang, J.; Yu, H.-Q. Photocatalytic degradation of bisphenol A by oxygen-rich and highly visible-light responsive  $\text{Bi}_{12}\text{O}_{17}\text{Cl}_2$  nanobelts. *Appl. Catal., B* **2017**, *200*, 659.
- (37) Li, B.; Shao, L.; Zhang, B.; Wang, R.; Zhu, M.; Gu, X. Understanding size-dependent properties of BiOCl nanosheets and exploring more catalysis. *J. Colloid Interface Sci.* **2017**, *505*, 653.
- (38) Sun, Y.; Zhao, Z.; Dong, F.; Zhang, W. Mechanism of visible light photocatalytic  $\text{NO}_x$  oxidation with plasmonic Bi cocatalyst-enhanced  $(\text{BiO})_2\text{CO}_3$  hierarchical microspheres. *Phys. Chem. Chem. Phys.* **2015**, *17*, 10383.
- (39) Ueda, W.; Iozaki, T.; Sakyu, F.; Nishiyama, S.; Morikawa, Y. Complex Metal Halide Oxides (1): Bismuth Chloride Oxides Having Various Structures as Catalysts for Oxidative Coupling of Methane. *Bull. Chem. Soc. Jpn.* **1996**, *69*, 485.
- (40) Chai, S. Y.; Kim, Y. J.; Jung, M. H.; Chakraborty, A. K.; Jung, D.; Lee, W. I. Heterojunctioned BiOCl/ $\text{Bi}_2\text{O}_3$ , a new visible light photocatalyst. *J. Catal.* **2009**, *262*, 144.
- (41) He, G.; Xing, C.; Xiao, X.; Hu, R.; Zuo, X.; Nan, J. Facile synthesis of flower-like  $\text{Bi}_{12}\text{O}_{17}\text{Cl}_2/\beta\text{-Bi}_2\text{O}_3$  composites with enhanced visible light photocatalytic performance for the degradation of 4-tert-butylphenol. *Appl. Catal., B* **2015**, *170–171*, 1.
- (42) Bi, C.; Cao, J.; Lin, H.; Wang, Y.; Chen, S. BiOI/ $\text{Bi}_{12}\text{O}_{17}\text{Cl}_2$ : A novel heterojunction composite with outstanding photocatalytic and photoelectric performances. *Mater. Lett.* **2016**, *166*, 267.
- (43) Grice, J. D. A solution to the crystal structures of bismutite and beyerite. *Can. Mineral.* **2002**, *40*, 693.
- (44) Lagerkrantz, A.; Sillén, L. G. On the crystal structure of  $\text{Bi}_2\text{O}_2\text{CO}_3$  (bismutite) and  $\text{CaBi}_2\text{O}_2(\text{CO}_3)_2$  (beyerite). *Ark. Kemi, Mineral. Geol.* **1947**, *A25*, 1.
- (45) Taylor, P.; Sunder, S.; Lopata, V. J. Structure, spectra, and stability of solid bismuth carbonates. *Can. J. Chem.* **1984**, *62*, 2863.
- (46) Nurgaliev, B. Z.; Popovkin, B. A.; Stefanovich, S. Y. New bismuth oxide bromides and oxide chlorides. *Russ. J. Inorg. Chem.* **1983**, *28*, 2207.
- (47) Chen, X. Y.; Huh, H. S.; Lee, S. W. Controlled synthesis of bismuth oxo nanoscale crystals ( $\text{BiOCl}$ ,  $\text{Bi}_{12}\text{O}_{17}\text{Cl}_2$ ,  $\alpha\text{-Bi}_2\text{O}_3$ , and  $(\text{BiO})_2\text{CO}_3$ ) by solution-phase methods. *J. Solid State Chem.* **2007**, *180*, 2510.
- (48) Tien, L.-C.; Lin, Y.-L.; Chen, S.-Y. Synthesis and characterization of  $\text{Bi}_{12}\text{O}_{17}\text{Cl}_2$  nanowires obtained by chlorination of  $\alpha\text{-Bi}_2\text{O}_3$  nanowires. *Mater. Lett.* **2013**, *113*, 30.
- (49) Lu, H.; Xu, L.; Wei, B.; Zhang, M.; Gao, H.; Sun, W. Enhanced photosensitization process induced by the p–n junction of  $\text{Bi}_2\text{O}_2\text{CO}_3/\text{BiOCl}$  heterojunctions on the degradation of rhodamine B. *Appl. Surf. Sci.* **2014**, *303*, 360.
- (50) Xiao, X.; Liu, C.; Hu, R.; Zuo, X.; Nan, J.; Li, L.; Wang, L. Oxygen-rich bismuth oxyhalides: generalized one-pot synthesis, band structures and visible-light photocatalytic properties. *J. Mater. Chem.* **2012**, *22*, 22840.
- (51) Zheng, Y.; Duan, F.; Chen, M.; Xie, Y. Synthetic  $\text{Bi}_2\text{O}_2\text{CO}_3$  nanostructures: novel photocatalyst with controlled special surface exposed. *J. Mol. Catal. A: Chem.* **2010**, *317*, 34.
- (52) Huang, H.; Wang, J.; Dong, F.; Guo, Y.; Tian, N.; Zhang, Y.; Zhang, T. Highly efficient  $\text{Bi}_2\text{O}_2\text{CO}_3$  single-crystal lamellas with dominantly exposed {001} facets. *Cryst. Growth Des.* **2015**, *15*, 534.
- (53) Liu, Y.; Wang, Z.; Huang, B.; Yang, K.; Zhang, X.; Qin, X.; Dai, Y. Preparation, electronic structure, and photocatalytic properties of  $\text{Bi}_2\text{O}_2\text{CO}_3$  nanosheet. *Appl. Surf. Sci.* **2010**, *257*, 172.
- (54) Moulder, J. F.; Stickle, W. F.; Sobol, P. E.; Bomben, K. D. *Handbook of X-ray Photoelectron Spectroscopy*; PerkinElmer Corporation: Eden Prairie, MN, 1992.
- (55) Armelao, L.; Bottaro, G.; Maccato, C.; Tondello, E. Bismuth oxychloride nanoflakes: Interplay between composition–structure and optical properties. *Dalton Trans.* **2012**, *41*, 5480.
- (56) Strohmeier, B. R. Evaluation of polymeric standard reference materials for monitoring the performance of X-ray photoelectron spectrometers. *Appl. Surf. Sci.* **1991**, *47*, 225.
- (57) Yagub, M. T.; Sen, T. K.; Afroze, S.; Ang, H. M. Dye and its removal from aqueous solution by adsorption: A review. *Adv. Colloid Interface Sci.* **2014**, *209*, 172.
- (58) Li, W.; Xiao, F.; Su, H.; Wang, D.; Yang, X. Investigation of adsorption and photocatalytic activities of in situ cetyltrimethylammonium bromide-modified Bi/BiOCl heterojunction photocatalyst for organic contaminants removal. *RSC Adv.* **2016**, *6*, 93309.
- (59) Obregón, S.; Colón, G. On the different photocatalytic performance of  $\text{BiVO}_4$  catalysts for Methylene Blue and Rhodamine B degradation. *J. Mol. Catal. A: Chem.* **2013**, *376*, 40.
- (60) Pan, C.; Xu, J.; Chen, Y.; Zhu, Y. Influence of OH-related defects on the performances of  $\text{BiPO}_4$  photocatalyst for the degradation of rhodamine B. *Appl. Catal., B* **2012**, *115–116*, 314.
- (61) Konstantinou, I. K.; Albanis, T. A.  $\text{TiO}_2$ -assisted photocatalytic degradation of azo dyes in aqueous solution: kinetic and mechanistic investigations: A review. *Appl. Catal., B* **2004**, *49*, 1.
- (62) Yu, J.; Wei, B.; Zhu, L.; Gao, H.; Sun, W.; Xu, L. Flowerlike C-doped BiOCl nanostructures: Facile wet chemical fabrication and enhanced UV photocatalytic properties. *Appl. Surf. Sci.* **2013**, *284*, 497.
- (63) Hameed, A.; Montini, T.; Gombac, V.; Fornasiero, P. Surface Phases and Photocatalytic Activity Correlation of  $\text{Bi}_2\text{O}_3/\text{Bi}_2\text{O}_{4-x}$  Nanocomposite. *J. Am. Chem. Soc.* **2008**, *130*, 9658.